Research Article

Low concentration isopropanol gas sensing properties of Ag nanoparticles decorated In$_2$O$_3$ hollow spheres

Chao ZHANG[a,*], Yunchun HUAN[a], Ying LI[a], Yifan LUO[a,b], Marc DEBLIQUY[b]

[a]*College of Mechanical Engineering, Yangzhou University, Yangzhou 225127, China*
[b]*Materials Science Department, University of Mons, Mons 7000, Belgium*

©The Author(s) 2021.

Abstract: In order to detect low concentrations of volatile organic compounds (VOCs) for the early diagnosis of lung cancer, sensors based on hollow spheres of In$_2$O$_3$ were prepared through the soft template method. Ag nanoparticle decorated In$_2$O$_3$ composites were synthesized via dipping and annealing. The microstructure, phase composition, element distribution, and state of Ag were analyzed by the scanning electron microscopy (SEM), X-ray diffraction (XRD), high-resolution transmission electron microscopy (HRTEM), and X-ray photoelectron spectroscopy (XPS). The gas sensing tests showed that Ag–In$_2$O$_3$ sensors had the highest response to isopropanol at 300 ℃. The best response of Ag–In$_2$O$_3$ composite sensor was 5.2, which had a significant improvement compared with only In$_2$O$_3$. Moreover, the response and recovery time of Ag–In$_2$O$_3$ composite sensor was significantly shortened. The improved sensing properties of Ag–In$_2$O$_3$ composite sensor could be attributed to the Schottky barrier created at Ag–In$_2$O$_3$ interface and catalytical effect of Ag.

Keywords: Ag–In$_2$O$_3$; hollow spheres; isopropanol; gas sensor

1 Introduction

Lung cancer is one of the most common cancers [1]. Although some progress has been made recently in the medical field, the mortality rate of lung cancer patients remains high for a long time [2]. Some drugs and special types of treatments can alleviate patients' pain and prolong the survival time of patients, but the chances of a complete cure are very low [3]. If lung cancer can be diagnosed at an early stage, the medical effect will be significantly improved. Indeed, the lung cancer survival chance is about 15%–20% for most patients within 5 years. However, if lung cancer is detected at an early stage, the survival chance can be increased to around 80% [4]. At present, the most common diagnostic methods for lung cancer are computed tomography (CT) and biopsy, but they have side effects on patients and are considered as invasive methods. In addition, the early symptoms of lung cancer are very insidious and thus the misdiagnosis rate of these methods is relatively high [5]. Therefore, the lack of early diagnosis is an extremely important because of high lung cancer mortality in all cancers [6]. Harmless, simple, and accurate lung cancer detection methods need to be developed urgently.

In the exhaled breath of humans, the concentration of some volatile organic compounds (VOCs) has been an important characteristic marker for the detection of lung cancer patients [7,8]. It is a suitable non-invasive method for clinical diagnosis. Some of the hydrocarbons,

* Corresponding author.
E-mail: zhangc@yzu.edu.cn, zhangchao_cqu@hotmail.com

alcohols, aldehydes, and ketones are considered as biomarkers of cancer [9]. So far, there is no clear list of gases that are unambiguously biomarkers for lung cancer. However, among the possible VOCs, it has been reported that the highest concentration of isopropanol in exhaled breath of lung cancer patients is about 1 ppm and the average concentration is about 400 ppb, which is more than twice the value of healthy people [10–12]. Monitoring the concentration of VOCs exhaled by patients can provide some evidence for the early diagnosis of patients. As a result, it is of great significance to develop an efficient detection technique for low concentration isopropanol (< 5 ppm).

The concentration of most VOCs in exhaled breath is low (usually below 1 ppm), so that equipment with high sensitivity is necessary for the detection [12]. The general VOC detection methods include gas chromatography–mass spectrometry (GC–MS) [13,14], ion mobility spectrometry (IMS) [15], gold nanoparticle sensor array [16], and semiconductor metal oxide sensor [17,18]. Among them, semiconductor metal oxide sensor has a good prospect for VOC detection because of its great sensitivity, fast response, lower cost, as well as simple fabrication [19,20]. Metaloxide sensors (MOSs) consist of an insulating substrate fitted with a pair of electrodes covered with a semiconducting metal oxide as the sensitive layer [21,22]. The sensing mechanism is that gases can be reversibly adsorbed on the surface of the sensitive layer and electron transfers can be provoked when the interaction between the semiconductor and gases is intense enough. The reaction process will lead to the modification of the charge carrier concentration and then the conductivity of the semiconductor changes. According to the adsorption–desorption equilibrium, there is a link between the conductivity of the sensitive layer and the gas concentration. The detection signal is just the change of resistance among the electrodes (usually interdigitated electrodes). To work properly (speed up the surface reactions), the sensitive layer has to operate at high temperatures (typically in the range of 150–500 ℃) [23,24]. With enabling wide-ranging electrical functionality, indium oxide has an excellent prospect and it has been widely studied and applied in VOC gas sensors, owing to its excellent properties, including high sensitivity, large bandgap (3.65 eV), good chemical stability, low cost, and non-toxicity [25–27]. The morphology of sensing materials strongly affects gas sensing performance [28,29]. Some researchers have proved that In_2O_3 materials with large specific surface areas, especially the hollow structure, can improve the response performance of semiconductors to the target gas [30]. The hollow structure is conducive to the adsorption and desorption of gas and produces more active reaction sites for the gas sensor [31,32].

In addition, the decoration of noble metals on metal oxides also plays an important method in improving gas sensing performance [33]. The commonly used noble metals include Pt, Ag, Au, Pd, etc. [34,35]. Yang *et al*. [36] synthesized Au decorated In_2O_3 hollow nanospheres via the hydrothermal method. The response (defined as the value of the senor resistance in air divided by the sensor resistance in the presence of the target gas) of 5 wt% Au–In_2O_3 to 100 ppm 1-butylamine was 26.3, which was 9 times that of pure In_2O_3. At the same time, the optimal working temperature and response time are decreased. Liu *et al*. [37] found that the decorating of Pt nanoparticles on In_2O_3 hollow spheres can effectively improve the acetone sensing performance. From the experimental results, Pt–In_2O_3 sensor had the best gas sensing performance when the In/Pt atomic ratio was 26. The Pt–In_2O_3 composite sensor exhibits a much higher response (15.1 for 1 ppm acetone) than pure In_2O_3 (5.1 for 1 ppm acetone). The improvement of performance is mainly attributed to the following two factors. Firstly, oxygen molecules were more effectively bound and dissociated with the catalysis of Pt. Secondly, due to the different Fermi energy between Pt and In_2O_3, a Schottky barrier was formed and the width of interfacial electron depletion layer increased. Hence, the change of sensor resistance was more obvious in the process of gas sensing response. Inspired by these, we chose Ag to decorate In_2O_3 to further improve its gas sensing performance. Ag has high electrical conductivity thermal conductivity, antibacterial characteristics, and nontoxicity [38]. The lower Fermi level makes it easy to form a Schottky barrier with In_2O_3. Compared with other similar noble metals, Ag is more attractive because of much lower cost (no more than 2% cost of the Au, Pd, and Pt). From the viewpoint of practical application in this paper, it is significant to cut the cost of the sensing materials.

In this study, a composite soft template method and a condensation reflux method were utilized to synthesize In_2O_3 hollow spheres. And then, Ag decorated In_2O_3 in different atomic ratios were synthesized by dipping in

AgNO$_3$ solution and annealing. The best loading atomic ratio of Ag nanoparticles and the optimal working temperature are investigated to elevate the sensing properties of In$_2$O$_3$ based sensors. The mechanism of the promoted sensing properties of Ag–In$_2$O$_3$ composites is studied.

2　Experimental

2. 1　Synthesis of In$_2$O$_3$ hollow spheres

As shown in Fig. 1, 3.2 g DL-aspartic acid was completely dissolved in 360 mL prepared deionized water at 60 ℃ and then 400 mL 0.1 mol/L PEG-4000 aqueous solution was added to form micelles. After magnetic stirring for 30 min, the composite soft template was synthesized and made to form a uniform suspension. Then, 24.024 g of urea and 80 mL 0.2 mol/L In(NO$_3$)$_3$ aqueous solution were added into the mixture. The above mixture was heated with magnetic stirring until it boiled slightly for 3 h via the condensation reflux method. Owing to the electrostatic adsorption between the composite soft template and the metal cations In^{3+}, the In^{3+} cations gathered around the template. So the metal ions were precipitated on the surface of template with OH$^-$ which was formed by urea under high temperatures. Finally, In(OH)$_3$ precursor with a hollow sphere structure was prepared. After cooling and deposition, the white precipitate was washed six times with deionized water. After drying at 100 ℃ for 24 h, the precipitate was annealed at 500 ℃ for 2 h to obtain pure In$_2$O$_3$ hollow spheres.

2. 2　Synthesis of Ag–In$_2$O$_3$

As shown in Fig. 1, 0.139 g In$_2$O$_3$ powders were added to 10 mL of deionized water to form a suspension and then different volumes of 0.085 mol/L AgNO$_3$ solutions were added. After ultrasonic treatment processing for 20 min, the uniform suspension (in an open vessel) was annealed at 300 ℃ for 2 h under a nitrogen atmosphere. By heating, the gradually precipitated AgNO$_3$ would decompose into Ag, NO$_2$, and O$_2$ with the evaporation of water [39]. Then, six different Ag/In atomic ratios (1, 2, 3, 4, 5, and 6) of Ag decorated In$_2$O$_3$ powders were synthesized, which were named as 1Ag–In, 2Ag–In, 3Ag–In, 4Ag–In, 5Ag–In, and 6Ag–In, respectively.

2. 3　Characterization

The crystal information of Ag–In$_2$O$_3$ samples was determined by the X-ray diffractometer (XRD, Bruker D8 Advance, Germany) with a Cu Kα radiation at 2θ ranging from 20° to 80°. The morphologies of Ag–In$_2$O$_3$ were studied by the field-emission scanning electron microscope (FESEM, Hitachi S4800, Japan). The surface area of the material was evaluated using the Brunauer–Emmett–Teller (BET, BSD-PS2, China) method. The element composition, distribution, and lattice spacing of Ag–In$_2$O$_3$ were determined by the high-resolution transmission electron microscope (HRTEM, Tecnai G2 F30, the Netherlands). The X-ray photoelectron spectroscope (XPS, ESCALAB 250Xi, USA) also examined the chemical composition and element distribution of Ag–In$_2$O$_3$.
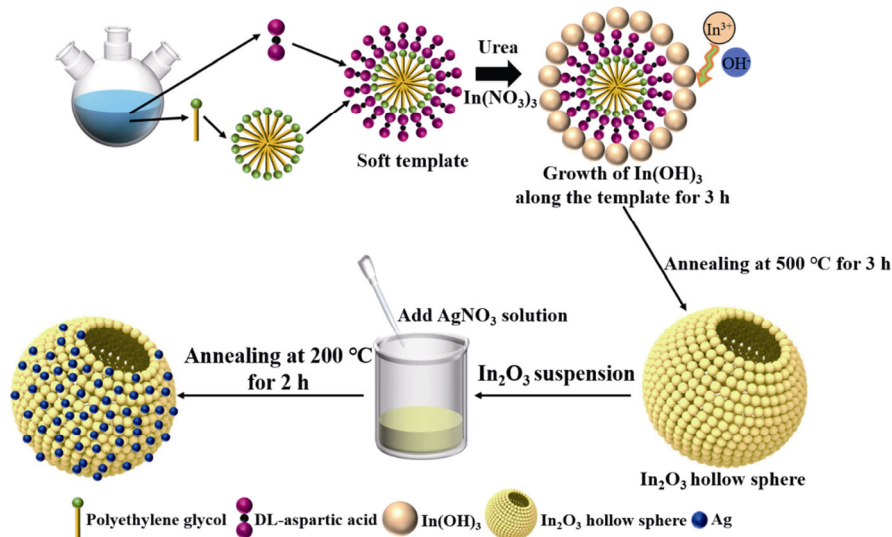

Fig. 1　Synthesis steps of Ag nanoparticle-decorated In$_2$O$_3$ hollow spheres.

2. 4   Gas sensing equipment

The seven groups of samples, including In_2O_3, 1Ag–In, 2Ag–In, 3Ag–In, 4Ag–In, 5Ag–In, and 6Ag–In, were stirred in deionized water to obtain uniform paste separately. Then the seven pastes were coated on seven Al_2O_3 substrates uniformly by a small brush. The substrates were equipped with interdigital Pt electrodes to measure the resistance and heat sensor. After being dried at 100 ℃ for 24 h, these prepared sensors were installed in a four-channel gas sensing testing device. The testing device is shown in Fig. 2. Firstly, a suitable amount of liquid isopropanol is injected into the heating table in the gas chamber. Then under the action of fans and heating, isopropanol gasified rapidly and filled the gas chamber to form the target gas. The target gas was extracted by the gas pump to form a closed loop between the test chamber and the gas chamber for the implementation of gas sensing experiment. The computer can directly control the temperature of each sensor and the flow of gas flowmeter. Before the gas sensing test, the sensor needed to be stabilized at 300 ℃ for 1 h in the air environment. The sensor responses is defined in Eq. (1):

$$S = (R_a - R_g)/R_g \times 100\% \qquad (1)$$

where R_a is the stable resistance value of the gas sensor in air and R_g is the stable resistance value of the gas sensor in contact with the testing gases.

3   Results and discussion

3. 1   Structure characterization

The XRD patterns of In_2O_3, 1Ag–In, 2Ag–In, 3Ag–In, 4Ag–In, 5Ag–In, and 6Ag–In are shown in Fig. 3. The six main peaks of cubic-structure In_2O_3 refer to planes of (222), (400), (411), (332), (431), and (440) of In_2O_3 [40]. Based on the Debye–Scherrer formula calculation, the In_2O_3 average crystal size of seven samples was about 15 nm. When the Ag content is low, no obvious Ag diffraction peak can be observed. When samples' Ag/In atomic ratio is greater than three, two peaks of cubic-structure Ag at 38.11° and 44.28° are observed, which could correspond to (111) and (200) planes of cubic Ag, respectively [41]. Therefore, XRD patterns indicate that Ag was successfully loaded on the In_2O_3. Since no other peaks appear, the purity of the samples is high.

The SEM micrographs of the seven Ag–In_2O_3 samples are shown in Fig. 4 and the insets are corresponding to high magnification images of each sample. It is observed from Fig. 4(a) that pure In_2O_3 has obvious hollow sphere morphology with about 900 nm in diameter. Through the high magnification images, the hollow spheres with a porous structure are mainly composed of nanoparticles. From Figs. 4(b)–4(g), the content of Ag increases. The silver decoration has little effect on the morphology and hollow spheres maintain the original structure of pure In_2O_3. From high magnification images, after the decorating of Ag, some nanoparticles are added to the surface of hollow spheres. Compared with pure In_2O_3, these Ag–In_2O_3 hollow spheres have a rougher surface. To further achieve the information about specific surface area, the N_2 adsorption and desorption of 5Ag–In are measured in Fig. 5. The specific surface area of 48.935 m^2/g is calculated by the BET method.

The microstructure and composition of Ag–In_2O_3 were executed by HRTEM. Figure 6 shows the HRTEM image of 5Ag–In and the translucent region in the sphere
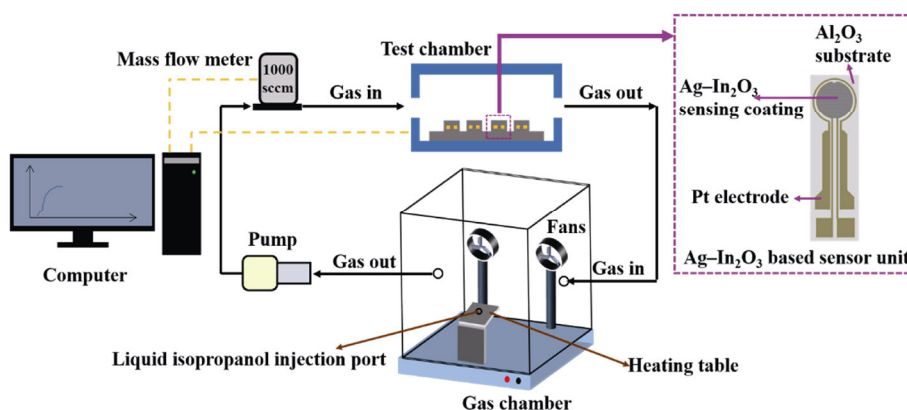

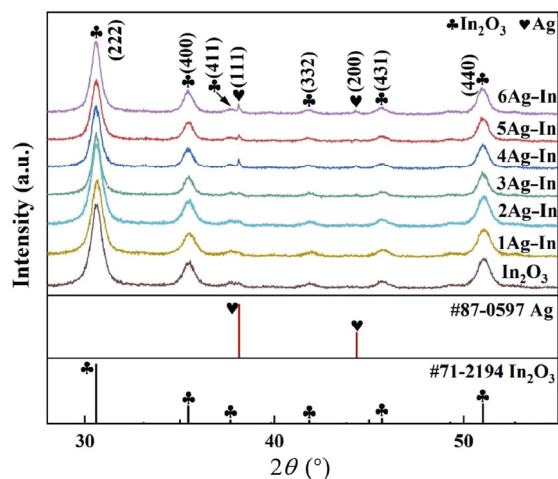**Fig. 2**   Details of the gas sensing testing system.

Fig. 3 XRD patterns of In$_2$O$_3$, 1Ag–In, 2Ag–In, 3Ag–In, 4Ag–In, 5Ag–In, and 6Ag–In.

can be observed, which proves the hollow sphere structure. A large number of nanoparticles are assembled into a hollow spherical shell and the surface of the sphere is also dispersed with discrete small particles. The diameter of the hollow sphere is about

1000 nm, which matches up with the SEM images. Therefore, the decorating of Ag did not destroy the hollow sphere structure. To verify the existence of decorating Ag on the hollow sphere, the EDS surface scanning of 5Ag–In (Cu substrate) was carried out. As shown in energy dispersive X-ray spectrum (EDS) and mappings of 5Ag–In in Fig. 6, the powder has three elements, i.e., O, In, and Ag. Ag nanoparticles were massively distributed on the shell of In$_2$O$_3$ microspheres. As revealed in the lattice image, the lattice fringes of 0.287 nm were assigned to the (222) plane of In$_2$O$_3$, while 0.236 nm of the lattice fringes can correspond with the Ag (111) plane spacing on an Ag nanoparticle [41]. The above results indicate that Ag nanoparticles are decorated on hollow spheres indeed.

For further investigation on the sample's elemental composition and chemical state of Ag decorated on In$_2$O$_3$ hollow spheres, the 5Ag–In was also analyzed by XPS. As shown in Fig. 7(a), O, C, In, and Ag elements were identified in the XPS survey, and no obvious impurity peaks appeared, indicating that the
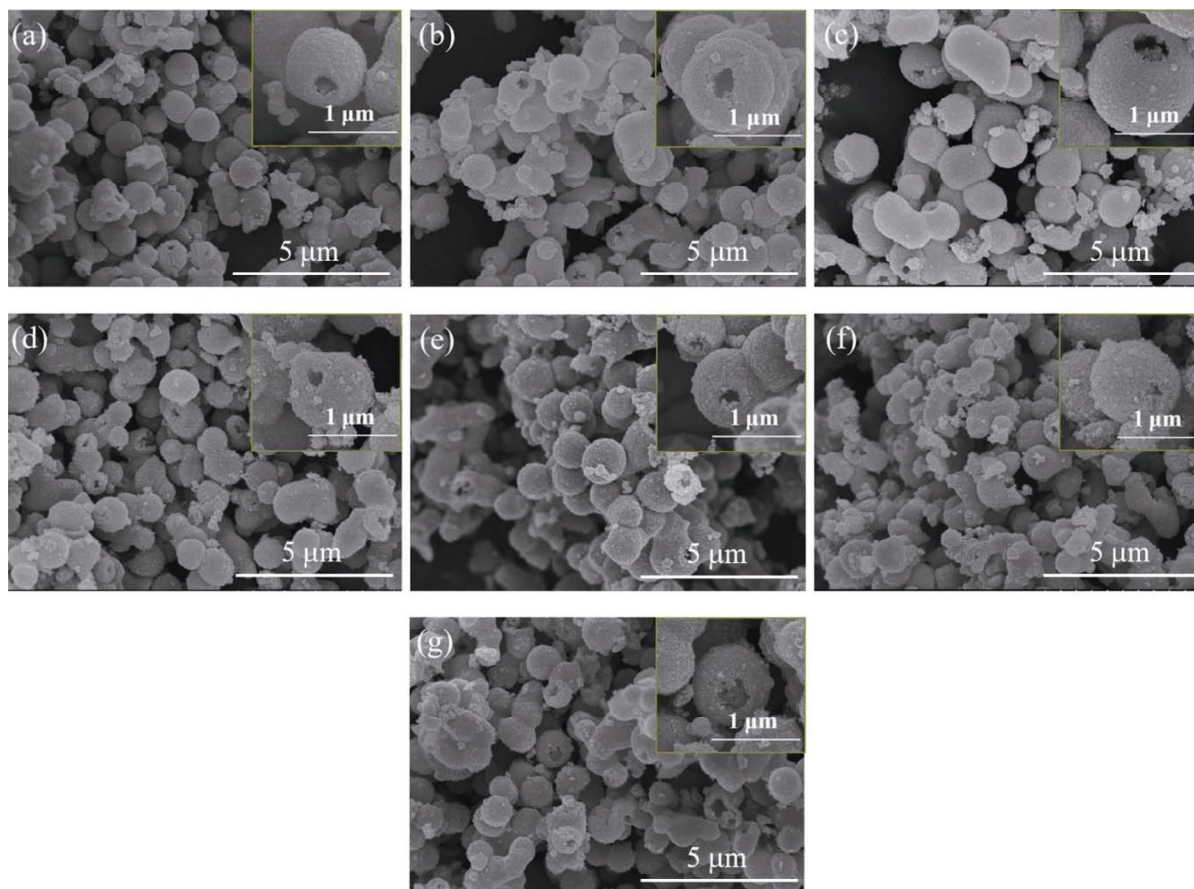

Fig. 4 SEM images of (a) In$_2$O$_3$, (b) 1Ag–In, (c) 2Ag–In, (d) 3Ag–In, (e) 4Ag–In, (f) 5Ag–In, and (g) 6Ag–In samples (the insets are the corresponding high magnification images).
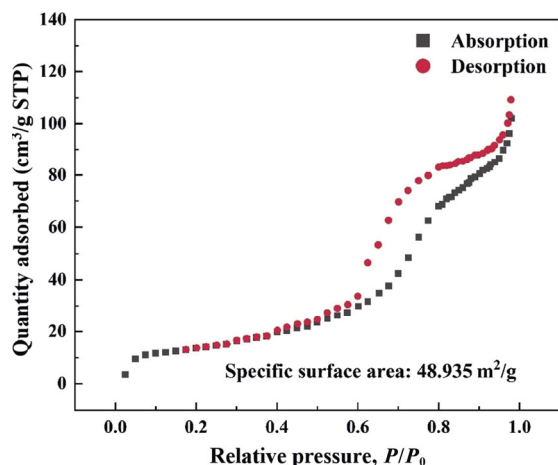
Fig. 5 Typical N$_2$ adsorption–desorption isotherm of 5Ag–In.

high purity of the 5Ag–In. Figure 7(b) shows the In 3d spectra. The double shoulder diffraction peaks at 444.8 and 452.4 eV correspond to characteristic peaks of cubic In$_2$O$_3$ [42]. In the O 1s spectra of Fig. 7(c), the peaks at 531.1 and 529.5 eV correspond to the oxygen vacancy and lattice oxygen, respectively [42]. From Fig. 7(d), the Ag 3d spectrum consists of two banding energy peaks of Ag, including Ag 3d$_{3/2}$ at 374.0 eV and Ag 3d$_{5/2}$ at 368.0 eV, which are corresponding to the

valence of Ag element [43]. For metallic Ag, Ag 3d$_{5/2}$ peak appears at 368.0–368.2 eV. And the Ag 3d$_{5/2}$ peak of Ag$^+$ in Ag$_2$O appears at about 367.7 eV [44]. Therefore, the state of Ag in the sample is metallic. Based on the above XRD, XPS, and HRTEM experimental outcomes, the Ag nanoparticles are successfully decorated.

3. 2　Isopropanol sensing performance

To explore the optimized operating temperature of the sensor, the responses of seven sensors to 5 ppm isopropanol at 150–400 ℃ are shown in Fig. 8. The responses of all sensors were low at 150 ℃. It may be attributed to the slow reaction rate of the reducing gas and low activation energy of the gas sensing layer surface under low temperatures. With the increase in temperature (150–300 ℃), the sensor response improved significantly. At this stage, the amount of target gas adsorbed on the gas sensing layer surface increased and the reaction was accelerated. Therefore, the response of all sensors reached the maximum value and the response of 5Ag–In gas sensor was 5.2 at 300 ℃. Under further increasing temperature, the desorption rate of target gas on the material surface was high, so the response of the sensor showed a
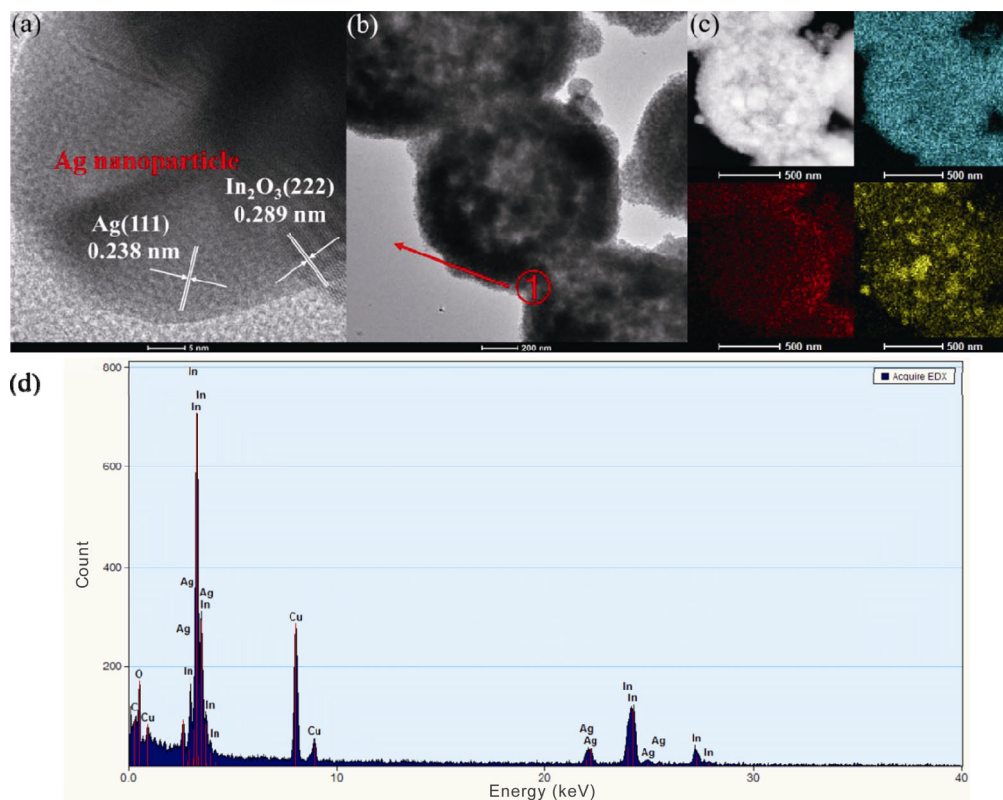

Fig. 6　(a) Lattice image, (b) HRTEM images, (c) the selected SEM image and the corresponding elemental mapping image, and (d) EDS mapping of 5Ag–In.
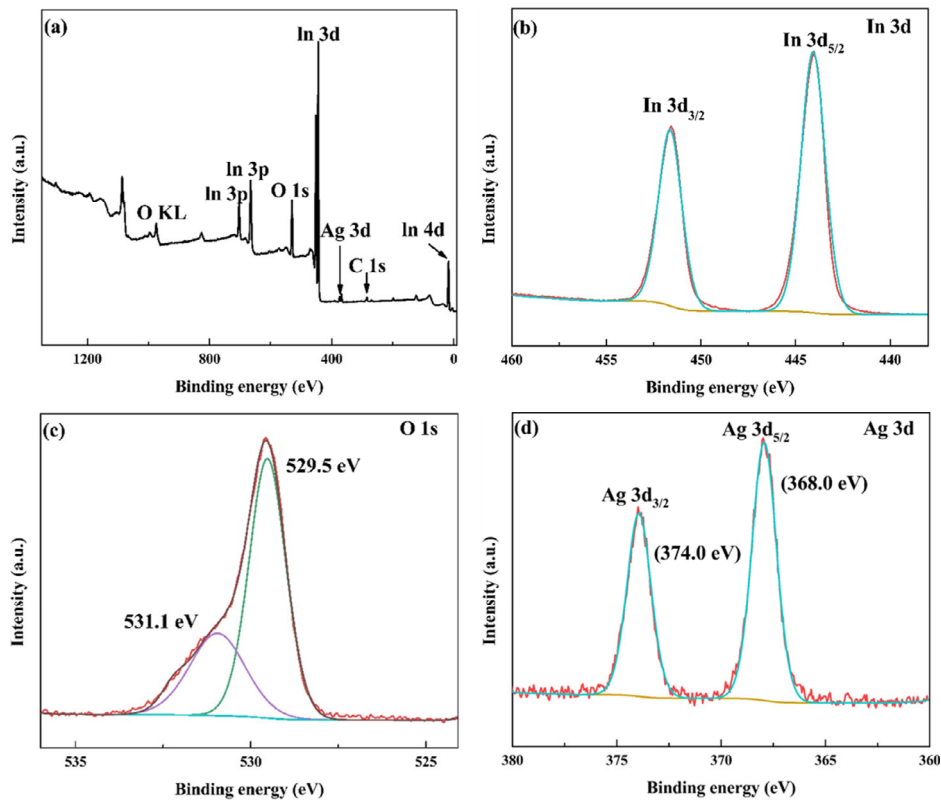
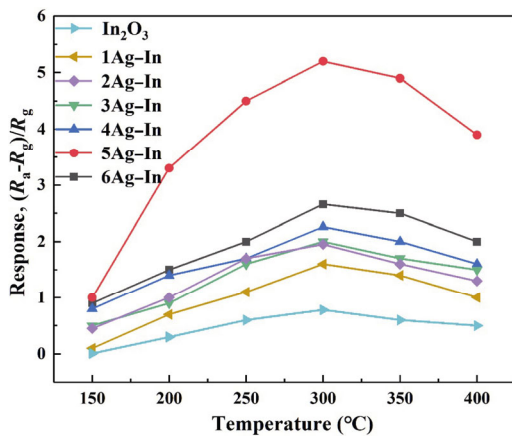**Fig. 7** XPS spectra of 5Ag–In: (a) full survey scan spectrum, (b) In 3d, (c) O 1s, and (d) Ag 3d.

Fig. 8 Sensor responses of seven Ag–In_2O_3 gas sensors towards 5 ppm isopropanol at 150–400 ℃.

downward trend [45]. Moreover, 5Ag–In has the best responses at different working temperatures. Therefore, 300 ℃ was selected as the best working temperature of all gas sensors, and the subsequent tests were carried out.

The real-time resistance changes of the seven sensors at 300 ℃ are shown in Fig. 9(a). With the injection of isopropanol, the resistance of seven sensors decreased obviously. Since isopropanol is a reducing gas, it showed that the Ag–In_2O_3 is n-type the

same as pure In_2O_3. The decoration of Ag improved the reference resistance of sensors and higher Ag content caused a higher reference resistance value. Figure 9(b) exhibits the dynamic response/recovery of seven sensors to 0.2–5 ppm isopropanol gas at 300 ℃. With the reduction of isopropanol concentration, the responses of all sensors decreased. The 5Ag–In gas sensor showed the best sensitivity under different concentrations of the target gas. Therefore, in addition to the microstructure of hollow spheres with large specific surface area, the sensitization of chemistry and electrons caused by the catalytic and great conductivity of Ag are also important reasons for enhancing gas sensitivity [41].

Figure 10 illustrates the seven sensors' responses to 0.2–5 ppm isopropanol at 300 ℃. Consistent with Fig. 9, the target gas concentration is proportional to the sensor response. Through the response of seven sensors at different concentrations of isopropanol, it can be concluded that the proportion of Ag nano-particles loaded increases with the atomic ratio of Ag loaded when the atomic ratio is less than 5. As the atomic ratio is more than 5, the sensitivity of the sensor begins to decrease. The responses of pure In_2O_3 sensors were 0.1, 0.3, 0.4, and 0.8 in 0.2–5 ppm
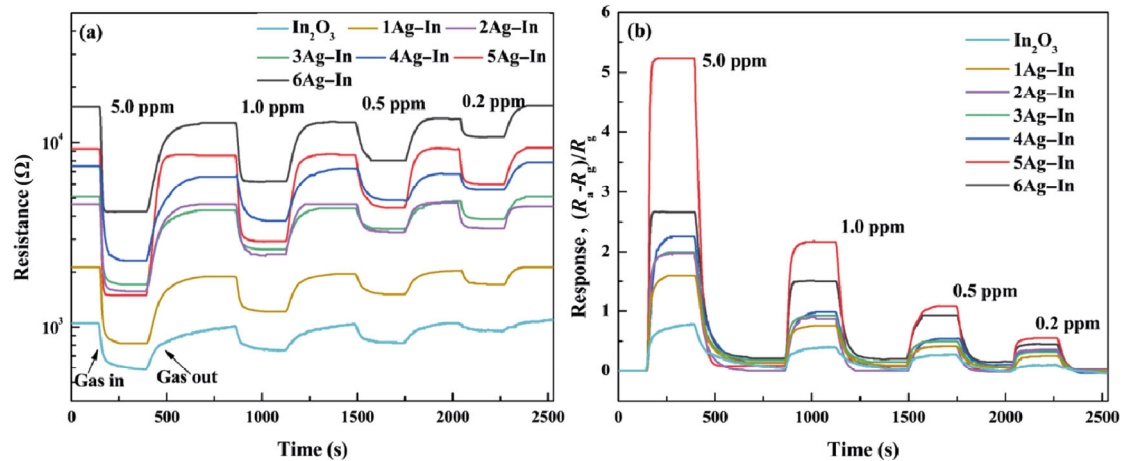
Fig. 9 (a) Real-time resistance change and (b) dynamic response curves of the seven sensors towards 0.2, 0.5, 1, and 5 ppm isopropanol at 300 ℃.
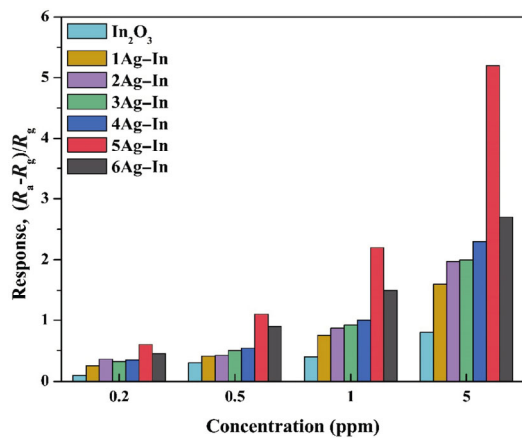

Fig. 10 Responses of the seven sensors to 0.2–5 ppm isopropanol at 300 ℃.

Fig. 11 Response/recovery time curves of In_2O_3 and 5Ag–In in sensors to 0.2–5 ppm isopropanol at 300 ℃.

isopropanol, while the responses of 5Ag–In were 0.6, 1.1, 2.2, and 5.2. The adornment of Ag improves sensors' properties, which was 6.5 times that of pure In_2O_3 at 5 ppm isopropanol.

Response and recovery time is also a key parameter of the sensor. In the process of target gas adsorption or desorption, the time required, when the sensor resistance change reaches 90% of the total change, is called response/recovery time. Figure 11 presents the response and recovery time of 5Ag–In and In_2O_3 sensors at 300 ℃ to different concentrations of isopropanol. By comparing the two groups of data, the response/ recovery time of the sensor was significantly shortened by decorating with Ag. The response/recovery time of pure In_2O_3 was 67 s/395 s to 1 ppm isopropanol, while those of 5Ag–In was 12 s/175 s, respectively. With the increasing isopropanol concentration, the sensor response time tends to decrease because fewer target gas molecules need a longer time to reach the equilibrium of
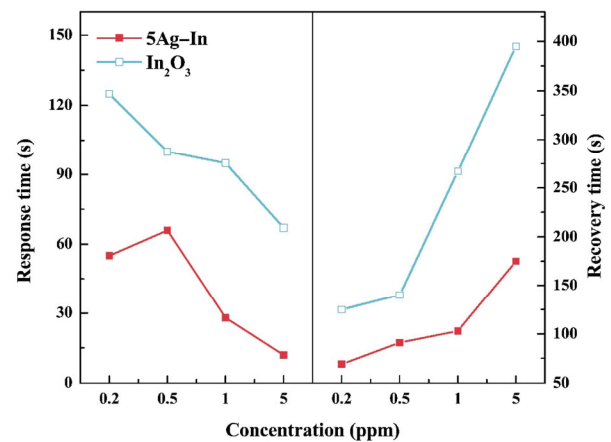
the reaction [46]. Based on the above phenomena, it can be concluded that Ag–In_2O_3 sensor has the best gas sensing performance when Ag/In atomic ratio is 5. Compared with pure In_2O_3, its response and response/ recovery rate were significantly improved. By decorating Ag, the performance and practicability of gas sensor can be effectively improved.

The selectivity to the target gas is another critical indicator of sensors. For evaluating the selectivity of Ag–In_2O_3 sensor, 5Ag–In sensor responses to 5 ppm ethanol, formaldehyde, acetone, and NH_3 at 300 ℃ are displayed in Fig. 12. The sensor responses to these interfering gases are 1.3, 1.5, 2.4, and 0.1, respectively, which are different from isopropanol. The difference origins from different adsorption and optimal reaction temperatures of the gas. However, it is obvious that the sensor still has a certain response to the other three VOC gases. Thus, it can be considered that the selectivity is not good to chemically similar VOCs.
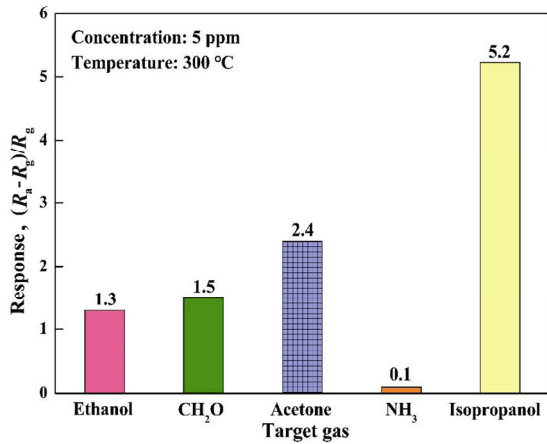
Fig. 12 Responses of 5Ag–In sensor to five different gases at 300 ℃.

Figure 13 illustrates the response/recovery curves of 5Ag–In gas sensor to 5 ppm isopropanol for 5 cycles at 300 ℃ after 60 days. The resistance could be well retained to its baseline after several sensing cycles, which indicates good reversibility of 5Ag–In sensor. Meanwhile, the response value did not change significantly during 5 response cycles of 5Ag–In sensor, indicating good stability of the sensor even after 60 days.

Moreover, the isopropanol sensitivity of our Ag–In_2O_3 sensor is compared with that of reported isopropanol sensors based on different metal oxides in other literature. As shown in Table 1, the limit detection concentration of most sensors is high (> 10 ppm). The prepared Ag–In_2O_3 composites show great isopropanol sensing properties at a low concentration level.
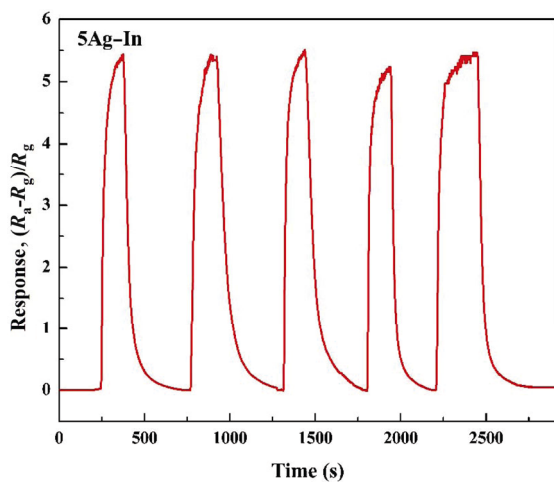

Fig. 13 Reversible response of 5Ag–In sensor to 5 ppm isopropanol at 300 ℃.
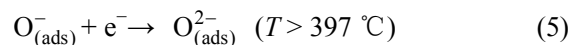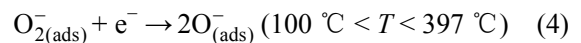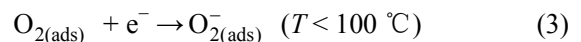
Table 1 Performance comparison of isopropanol sensors based on metal oxides

| Sensing material	Response	Concentration (ppm)	Temperature (℃)	Ref.
$ZnMn_2O_4$	1.28[a]	10	250	[47]
$ErFeO_3$	2.31[b]	2	270	[48]
CdS–ZnO	10.07[a]	10	350	[49]
SnO_2	7.27[a]	100	250	[50]
ZnO–CdO	4.11[a]	100	248	[51]
SnO_2@SiC	2.6[a]	100	500	[52]
Ag–In_2O_3	2.2[c] (3.2[a])	1	300	This work

[a] $S = R_a/R_g$; [b] $S = R_g/R_a$; [c] $S = (R_a - R_g)/R_g$.

3.3 Gas sensing mechanism

In general, the principle of metal oxide gas sensors needs oxygen ion adsorption theory to explain its surface resistance control model [53,54]. In_2O_3 is a n-type semiconductor because of the presence of oxygen vacancies that act as electron donors. In the air, the surface of the In_2O_3 gas sensing layer will absorb oxygen molecules. These oxygen molecules capture electrons from the semiconductors, which produce adsorbed oxygen ions and an electron depletion layer (Fig. 14(a)). The type of adsorbed oxygen ions (O_2^-, O^-, or O^{2-}) is also affected by the environmental temperature (T) [36]. The decrease in the concentration of free electrons increases the sensor resistance. The reactions process on the surface are shown in Eqs. (2)–(5) [55,56]:

$$O_{2(gas)} \rightarrow O_{2(ads)} \tag{2}$$

$$O_{2(ads)} + e^- \rightarrow O_{2(ads)}^- \quad (T < 100\ ℃) \tag{3}$$

$$O_{2(ads)}^- + e^- \rightarrow 2O_{(ads)}^- \ (100\ ℃ < T < 397\ ℃) \tag{4}$$

$$O_{(ads)}^- + e^- \rightarrow O_{(ads)}^{2-} \quad (T > 397\ ℃) \tag{5}$$

In this experiment, the best working temperature of sensor is 300 ℃, so the main oxygen ion is O^-. Once the sensor contacts isopropanol in the testing chamber, these isopropanol molecules will react with O^- ions. Meanwhile, the electrons trapped by oxygen return to the gas sensing layer. With the number of free electrons increasing, the resistance decreases. The global reaction of isopropanol with oxygen ions is shown in Eq. (6) [57]:

$$CH_3CH(OH)CH_3 + 9O^- \rightarrow 3CO_2 + 4H_2O + 9e^- \tag{6}$$
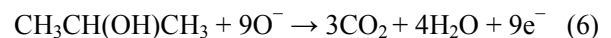
The reasons for the excellent performance of Ag–In_2O_3 can be summarized as follows. Firstly, the high specific surface area of the hollow sphere structure provides a large number of reaction sites for

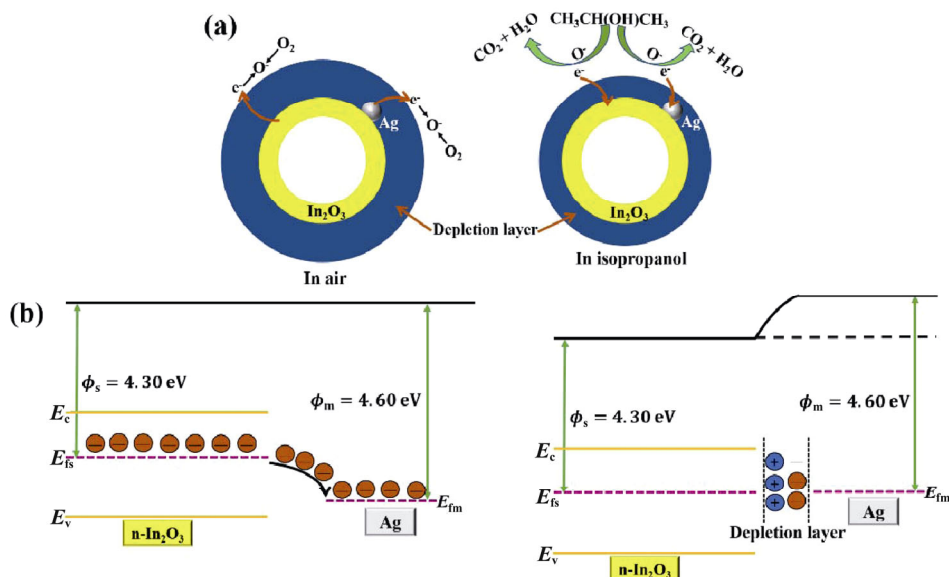**Fig. 14**   Schematic of (a) isopropanol sensing mechanism of the Ag–In$_2$O$_3$ and (b) band structure of the Ag–In$_2$O$_3$ composites (E_c, conduction band bottom; E_f, Fermi level; E_v, valence band top).

isopropanol response. Secondly, the work function of Ag (Φ_m = 4.6 eV) is larger than that of In$_2$O$_3$ (Φ_s = 4.3 eV) and its Fermi level (E_{fs}) is higher than that of Ag (E_{fm}). As a result, the band of In$_2$O$_3$ is bent via Ag decorating and the electrons are transferred from In$_2$O$_3$ to Ag to balance Fermi level, which forms a Schottky barrier and prevents the transmission of electrons [41,58,59]. So the electron depletion layer expands, as shown in Fig. 14(b). Reducing the number of electrons in In$_2$O$_3$ can benefit gas sensing because when fewer charge carriers are present, gas adsorption will capture the few remaining charge carriers near the surface and the sensor resistance will change dramatically [60]. Furthermore, as illustrated in Fig. 14(a), the transferred electrons in Ag nanoparticles are active, which can also react with oxygen in the air to produce more O$^-$ which increases the depletion again. The Schottky barrier and expanding electron depletion layer are also the main factors for the increase of sensor's reference resistance. Therefore, the more O$^-$ react with isopropanol, the more electrons are released in the process of sensor response. Then, the sensor resistance is reduced with the response improving significantly. Thirdly, Ag also functions as a catalyst. Due to Ag spillover effect, oxygen is adsorbed and dissociated more quickly and frequently [61,62], which increases the reaction rate with the isopropanol. While the response is improved, the process can effectively shorten the response/ recovery time. In general, increasing the Ag at% (< 5 at%) is beneficial for producing more active sites

and expanding the electron depletion layer of the sensor. However, excessive Ag clusters on the surface will decrease the number of chemical adsorption sites and thicken the hollow sphere shell, which is not conducive to the spread of gas molecules [42,63]. So the sensor response begins to decrease after the Ag/In atomic ratio exceeds 5%.

4   Conclusions

In this work, hollow sphere of In$_2$O$_3$ was prepared by the composite soft template method, and Ag was added into the composites by dipping and annealing to enhance the gas sensing performance. The 5 at% Ag–In$_2$O$_3$ showed the optimum sensitivity to isopropanol at 300 ℃. The response of Ag–In$_2$O$_3$ sensor (5.2) to 5 ppm isopropanol is about 6.5 times that of In$_2$O$_3$ sensor (0.8), and the Ag–In$_2$O$_3$ sensor response to 200 ppb isopropanol is 0.6. Meanwhile, the response/ recovery time of Ag–In$_2$O$_3$ was significantly shortened. The improvement of the sensor performance is mainly attributed to the hollow sphere structure, Schottky barrier between Ag nanoparticles and In$_2$O$_3$ hollow sphere, as well as the catalysis of Ag.

References

[1] Bray F, Ferlay J, Soerjomataram I, *et al*. Global cancer statistics 2018: GLOBOCAN estimates of incidence and mortality worldwide for 36 cancers in 185 countries. *CA*: *A Cancer J Clin* 2018, **68**: 394–424.

[2] Noreldeen HAA, Liu XY, Xu GW. Metabolomics of lung cancer: Analytical platforms and their applications. *J Sep Sci* 2020, **43**: 120–133.

[3] Gashimova E, Temerdashev A, Porkhanov V, *et al*. Investigation of different approaches for exhaled breath and tumor tissue analyses to identify lung cancer biomarkers. *Heliyon* 2020, **6**: e04224.

[4] Allemani C, Matsuda T, Di Carlo V, *et al*. Global surveillance of trends in cancer survival 2000-14 (CONCORD-3): Analysis of individual records for 37 513 025 patients diagnosed with one of 18 cancers from 322 population-based registries in 71 countries. *Lancet* 2018, **391**: 1023–1075.

[5] Fan Y, Noreldeen HAA, You L, *et al*. Lipid alterations and subtyping maker discovery of lung cancer based on nontargeted tissue lipidomics using liquid chromatography–mass spectrometry. *J Pharm Biomed Anal* 2020, **190**: 113520.

[6] Malvezzi M, Carioli G, Bertuccio P, *et al*. European cancer mortality predictions for the year 2017, with focus on lung cancer. *Ann Oncol* 2017, **28**: 1117–1123.

[7] Amann A, Ligor M, Ligor T, *et al*. Analysis of exhaled breath for screening of lung cancer patients. *Memo Mag Eur Med Oncol* 2010, **3**: 106–112.

[8] Sun X, Shao K, Wang T. Detection of volatile organic compounds (VOCs) from exhaled breath as noninvasive methods for cancer diagnosis. *Anal Bioanal Chem* 2016, **408**: 2759–2780.

[9] Xu H, Wei Y, Zhu L, *et al*. Bifunctional magnetic nanoparticles for analysis of aldehyde metabolites in exhaled breath of lung cancer patients. *J Chromatogr A* 2014, **1324**: 29–35.

[10] Rudnicka J, Walczak M, Kowalkowski T, *et al*. Determination of volatile organic compounds as potential markers of lung cancer by gas chromatography–mass spectrometry versus trained dogs. *Sens Actuat B*: *Chem* 2014, **202**: 615–621.

[11] Machado RF, Laskowski D, Deffenderfer O, *et al*. Detection of lung cancer by sensor array analyses of exhaled breath. *Am J Respir Crit Care Med* 2005, **171**: 1286–1291.

[12] Rudnicka J, Kowalkowski T, Buszewski B. Searching for selected VOCs in human breath samples as potential markers of lung cancer. *Lung Cancer* 2019, **135**: 123–129.

[13] Pesesse R, Stefanuto PH, Schleich F, *et al*. Multimodal chemometric approach for the analysis of human exhaled breath in lung cancer patients by TD–GC×GC–TOFMS. *J Chromatogr B Analyt Technol Biomed Life Sci* 2019, **1114–1115**: 146–153.

[14] Rudnicka J, Kowalkowski T, Ligor T, *et al*. Determination of volatile organic compounds as biomarkers of lung cancer by SPME–GC–TOF/MS and chemometrics. *J Chromatogr B Analyt Technol Biomed Life Sci* 2011, **879**: 3360–3366.

[15] Michalczuk B, Moravský L, Hrdá J, *et al*. Atmospheric pressure chemical ionisation study of selected volatile organic compounds (VOCs) by ion mobility spectrometry coupled with orthogonal acceleration time of flight mass spectrometry. *Int J Mass Spectrom* 2020, **449**: 116275.

[16] Bordbar MM, Tashkhourian J, Hemmateenejad B. Structural elucidation and ultrasensitive analyses of volatile organic compounds by paper-based nano-optoelectronic noses. *ACS Sens* 2019, **4**: 1442–1451.

[17] Chen XY, Wang XZ, Liu FJ, *et al*. Fabrication of porous Zn_2TiO_4–ZnO microtubes and analysis of their acetone gas sensing properties. *Rare Met* 2021, **40**: 1528–1535.

[18] Xu JY, Liu KW, Zhang C. Electronic nose for volatile organic compounds analysis in rice aging. *Trends Food Sci Technol* 2021, **109**: 83–93.

[19] Li Y, Lu YL, Wu KD, *et al*. Microwave-assisted hydrothermal synthesis of copper oxide-based gas-sensitive nanostructures. *Rare Met* 2021, **40**: 1477–1493.

[20] Liu D, Ren XW, Li YS, *et al*. Nanowires-assembled WO_3 nanomesh for fast detection of ppb-level NO_2 at low temperature. *J Adv Ceram* 2020, **9**: 17–26.

[21] Huan YC, Wu KD, Li CJ, *et al*. Micro-nano structured functional coatings deposited by liquid plasma spraying. *J Adv Ceram* 2020, **9**: 517–534.

[22] Wu KD, Xu JY, Debliquy M, *et al*. Synthesis and NH_3/TMA sensing properties of $CuFe_2O_4$ hollow microspheres at low working temperature. *Rare Met* 2021, **40**: 1768–1777.

[23] Zhao XH, Li ZZ, Lou XD, *et al*. Room-temperature chlorine gas sensor based on $CdSnO_3$ synthesized by hydrothermal process. *J Adv Ceram* 2013, **2**: 31–36.

[24] Zhang J, Liu XH, Neri G, *et al*. Nanostructured materials for room-temperature gas. *Adv Mater* 2016, **28**: 795–831.

[25] Zhang K, Qin S, Tang P, *et al*. Ultra-sensitive ethanol gas sensors based on nanosheet-assembled hierarchical ZnO–In_2O_3 heterostructures. *J Hazard Mater* 2020, **391**: 122191.

[26] Liu N, Li Y, Li YN, *et al*. Tunable NH_4F-assisted synthesis

of 3D porous In_2O_3 microcubes for outstanding NO_2 gas-sensing performance: Fast equilibrium at high temperature and resistant to humidity at room temperature. *ACS Appl Mater Interfaces* 2021, **13**: 14355–14364.

[27] Chethana DM, Thanuja TC, Mahesh HM, *et al*. Heterostructure Fe_2O_3–In_2O_3 nanoparticles as hydrogen gas sensor. *J Electron Mater* 2021, **50**: 4313–4323.

[28] Ma HN, Yu LM, Yuan X, *et al*. Room temperature photoelectric NO_2 gas sensor based on direct growth of walnut-like In_2O_3 nanostructures. *J Alloys Compd* 2019, **782**: 1121–1126.

[29] Zhou TT, Liu XP, Zhang R, *et al*. Shape control and selective decoration of Zn_2SnO_4 nanostructures on 1D nanowires: Boosting chemical-sensing performances. *Sens Actuat B*: *Chem* 2019, **290**: 210–216.

[30] Zhang DZ, Yang ZM, Li P, *et al*. Ozone gas sensing properties of metal-organic frameworks-derived In_2O_3 hollow microtubes decorated with ZnO nanoparticles. *Sens Actuat B*: *Chem* 2019, **301**: 127081.

[31] Liu H, Liu JY, Hong Z, *et al*. Preparation of hollow fiber membranes from mullite particles with aid of sintering additives. *J Adv Ceram* 2021, **10**: 78–87.

[32] Zhou TT, Zhang T, Zhang R, *et al*. Hollow $ZnSnO_3$ cubes with controllable shells enabling highly efficient chemical sensing detection of formaldehyde vapors. *ACS Appl Mater Interfaces* 2017, **9**: 14525–14533.

[33] Xu YS, Zheng W, Liu XH, *et al*. Facile Platinum single atoms on tin oxide ultrathin films for extremely sensitive gas detection. *Mater Hori* 2020,**7**: 1519–1527.

[34] Shen SK, Cui XL, Guo CY, *et al*. Sensing mechanism of Ag/α-MoO_3 nanobelts for H_2S gas sensor. *Rare Met* 2021, **40**: 1545–1553.

[35] Xu WJ, Zhang ZW, Liu CY, *et al*. Substantial thermoelectric enhancement achieved by manipulating the band structure and dislocations in Ag and La co-doped SnTe. *J Adv Ceram* 2021, **10**: 860–870.

[36] Yang XH, Fu HT, Tian Y, *et al*. Au decorated In_2O_3 hollow nanospheres: A novel sensing material toward amine. *Sens Actuat B*: *Chem* 2019, **296**: 126696.

[37] Liu W, Xie YL, Chen TX, *et al*. Rationally designed mesoporous In_2O_3 nanofibers functionalized Pt catalysts for high-performance acetone gas sensors. *Sens Actuat B*: *Chem* 2019, **298**: 126871.

[38] Zeng CY, Yuan L, Li XF, *et al*. Fabrication of urchin-like Ag/ZnO hierarchical nano/microstructures based on galvanic replacement mechanism and their enhanced photocatalytic properties. *Surf Interface Anal* 2017, **49**: 599–606.

[39] Yang WD, List-Kratochvil EJW, Wang CH. Metal particle-free inks for printed flexible electronics. *J Mater Chem C* 2019, **7**: 15098–15117.

[40] Xiao BX, Song SL, Wang P, *et al*. Promoting effects of Ag on In_2O_3 nanospheres of sub-ppb NO_2 detection. *Sens Actuat B*: *Chem* 2017, **241**: 489–497.

[41] Liu XJ, Sun XL, Duan XP, *et al*. Core–shell Ag@In_2O_3 hollow hetero-nanostructures for selective ethanol detection in air. *Sens Actuat B*: *Chem* 2020, **305**: 127450.

[42] Zhang C, Huan YC, Sun DJ, *et al*. Synthesis and NO_2 sensing performances of CuO nanoparticles loaded In_2O_3 hollow spheres. *J Alloys Compd* 2020, **842**: 155857.

[43] Ding MD, Xie N, Wang C, *et al*. Enhanced NO_2 gas sensing properties by Ag-doped hollow urchin-like In_2O_3 hierarchical nanostructures. *Sens Actuat B*: *Chem* 2017, **252**: 418–427.

[44] Schön G, Tummavuori J, Lindström B, *et al*. ESCA studies of Ag, Ag_2O and AgO. *Acta Chem Scand* 1973, **27**: 2623–2633.

[45] Luo YF, Ly A, Lahem D, *et al*. A novel low-concentration isopropanol gas sensor based on Fe-doped ZnO nanoneedles and its gas sensing mechanism. *J Mater Sci* 2021, **56**: 3230–3245.

[46] Wang TS, Zhang SF, Yu Q, *et al*. Novel self-assembly route assisted ultra-fast trace volatile organic compounds gas sensing based on three-dimensional opal microspheres composites for diabetes diagnosis. *ACS Appl Mater Interfaces* 2018, **10**: 32913–32921.

[47] Guillén-López ES, López-Urías F, Muñoz-Sandoval E, *et al*. High performance isopropanol sensor based on spinel $ZnMn_2O_4$ nanoparticles. *Mater Today Commun* 2021, **26**: 102138.

[48] Yang TT, Ma SY, Cao PF, *et al*. Synthesis and characterization of $ErFeO_3$ nanoparticles by a hydrothermal method for isopropanol sensing properties. *Vacuum* 2021, **185**: 110005.

[49] Zhang H, Jin Z, Xu MD, *et al*. Enhanced isopropanol sensing performance of the CdS nanoparticle decorated ZnO porous nanosheets-based gas sensors. *IEEE Sens J* 2021, **21**: 13041–13047.

[50] Li SH, Chu Z, Meng FF, *et al*. Highly sensitive gas sensor based on SnO_2 nanorings for detection of isopropanol. *J Alloys Compd* 2016, **688**: 712–717.

[51] Cai XY, Hu D, Deng SJ, *et al*. Isopropanol sensing properties of coral-like ZnO–CdO composites by flash preparation via self-sustained decomposition of metal-organic complexes. *Sens Actuat B*: *Chem* 2014, **198**: 402–410.

[52] Wang B, Wang YD, Lei YP, *et al*. Vertical SnO_2 nanosheet@SiC nanofibers with hierarchical architecture for high-performance gas sensors. *J Mater Chem C* 2016, **4**: 295–304.

[53] Tao ZH, Li YW, Zhang B, *et al*. Bi-doped urchin-like In_2O_3 hollow spheres: Synthesis and improved gas sensing and visible-light photocatalytic properties. *Sens Actuat B*: *Chem* 2020, **321**: 128623.

[54] Sadeghzadeh-Attar A. Photocatalytic degradation evaluation of N–Fe codoped aligned TiO_2 nanorods based on the effect of annealing temperature. *J Adv Ceram* 2020, **9**: 107–122.

[55] Dey A. Semiconductor metal oxide gas sensors: A review. *Mater Sci Eng*: *B* 2018, **229**: 206–217.

[56] Ma ZH, Yu RT, Song JM. Facile synthesis of Pr-doped In_2O_3 nanoparticles and their high gas sensing performance for ethanol. *Sens Actuat B*: *Chem* 2020, **305**: 127377.

[57] Jin Q, Wen W, Zheng SL, *et al*. Enhanced isopropanol

sensing of coral-like ZnO–ZrO$_2$ composites. *Nanotechnology,* 2020, **31**: 195502.

[58] Nirala G, Yadav D, Upadhyay S. Ruddlesden–Popper phase A$_2$BO$_4$ oxides: Recent studies on structure, electrical, dielectric, and optical properties. *J Adv Ceram* 2020, **9**: 129–148.

[59] Yang XH, Fu HT, Zhang LT, *et al*. Enhanced gas sensing performance based on the fabrication of polycrystalline Ag@TiO$_2$ core–shell nanowires. *Sens Actuat B*: *Chem* 2019, **286**: 483–492.

[60] Walker JM, Akbar SA, Morris PA. Synergistic effects in gas sensing semiconducting oxide nano-heterostructures: A review. *Sens Actuat B*: *Chem* 2019, **286**: 624–640.

[61] Xing RQ, Xu L, Song J, *et al*. Preparation and gas sensing properties of In$_2$O$_3$/Au nanorods for detection of volatile organic compounds in exhaled breath. *Sci Rep* 2015, **5**: 10717.

[62] Zhang C, Wu QD, Zheng BB, *et al*. Synthesis and acetone gas sensing properties of Ag activated hollow sphere structured ZnFe$_2$O4. *Ceram Int* 2018, **44**: 20700–20707.

[63] Zhang C, Sun DJ, Huan YC, *et al*. Highly sensitive ZnO nanoparticles-loaded In$_2$O$_3$ hollow microsphere for detecting ppb-level NO$_2$ at low working temperature. *Prog Nat Sci*: *Mater Int* 2020, **30**: 469–476.